Research Square

Preprints are preliminary reports that have not undergone peer review.
They should not be considered conclusive, used to inform clinical practice,
or referenced by the media as validated information.

Anthropogenic warming and urbanization accelerates the divergence between physical and emotional heat resilience

Shiqi Zhou

zhoushiqi@tongji.edu.cn

tongji university https://orcid.org/0009-0003-9068-4644

Weiyi jia

Tongji university

Yixuan Zou

Tongji university

Xiaodong Xu

Tongji university

Haowen Xu

School of Planning Building Environment, Technische Universität Berlin

Mo Wang

Guangzhou University https://orcid.org/0000-0001-8752-6256

Cong Guo

Beijing University of Technology

He Baojie

Chongqing University https://orcid.org/0000-0002-8841-0711

Pan feng

Southeast University

Zhangli Hu

Southeast University

Yongqi Lou

Tongji University

Fangzheng Li

School of Landscape Architecture, Beijing Forestry University

Jiaping Liu

Southeast University

Zhiqiang Wu

Tongji University

Hui Chen

Fuzhou University

Article

Keywords:

Posted Date: February 4th, 2026

DOI: https://doi.org/10.21203/rs.3.rs-8645964/v1

License: This work is licensed under a Creative Commons Attribution 4.0 International License.
Read Full License

Additional Declarations: There is **NO** Competing Interest.

Version of Record: A version of this preprint was published at Nature Climate Change on September 11th, 2026. See the published version at https://doi.org/10.1038/s41558-026-02732-8.

Anthropogenic warming and urbanization accelerates the divergence between physical and emotional heat resilience

Author names and affiliation:

Shiqi Zhou

a. College of Design and Innovation, Tongji University, Shanghai 200093, China

b. School of Materials Science and Engineering, Southeast University, Nanjing 211189, China

c. State Key Laboratory of Engineering Materials for Major Infrastructure, Jiangsu Sobute New Materials Co., Ltd., Nanjing, China

Email: zhoushiqi@tongji.edu.cn

Weiyi Jia

Address: China Shanghai Research Institute for Intelligent Autonomous Systems, Tongji University, Shanghai 200093, China

Email: jwy@tongji.edu.cn

Yixuan Zou

Address: China Shanghai Research Institute for Intelligent Autonomous Systems, Tongji University, Shanghai 200093, China

Email: yixuanzou@tongji.edu.cn

Xiaodong Xu

Address: China Shanghai Research Institute for Intelligent Autonomous Systems, Tongji University, Shanghai 200093, China

Email: xuxiaodong0901@tongji.edu.cn

Haowen Xu

Address:College of Architecture and Urban Planning, Tongji University, Shanghai 200093, China

Email: tjupxhw@tongji.edu.cn

Hui Chen

Address: School of Architecture and Urban-rural Planning, Fuzhou University, Fuzhou 350108,China

Email: chchenhui@fzu.edu.cn

Mo Wang

Address: College of Architecture and Urban Planning, Guangzhou University, Guangzhou 510006, China

Email: landwangmo@outlook.com

Cong Guo

Address: School of Architecture and Urban Planning, Beijing University of Technology , Beijing 100124, China

Email: congguo@bjut.edu.cn

Bao-Jie He

Address: Institute of Advanced Interdisciplinary Studies, Chongqing University, Chongqing, China

Email: baojie.he@cqu.edu.cn

Pan feng

Address: State Key Laboratory of Engineering Materials for Major Infrastructure, School of Materials Science and Engineering, Southeast University, Nanjing 211189, China

Email: pan.feng@seu.edu.cn

Zhangli Hu

a. School of Materials Science and Engineering, Southeast University, Nanjing 211189, China

b. State Key Laboratory of Engineering Materials for Major Infrastructure, Jiangsu Sobute New Materials Co., Ltd., Nanjing, China

Email:zhanglihu@seu.edu.cn

Yongqi Lou

College of Design and Innovation, Tongji University, Shanghai 200093, China

Email: louyongqi@tongji.edu.cn

Fangzheng Li

Address: School of Landscape Architecture, Beijing Forestry University, Beijing 100083, China

Email: fangzhengli@bjfu.edu.cn

Jiaping Liu

a. School of Materials Science and Engineering, Southeast University, Nanjing 211189, China

b. State Key Laboratory of Engineering Materials for Major Infrastructure, Jiangsu Sobute New Materials Co., Ltd., Nanjing, China

Email:ljp@cnjsjk.cn

Zhiqiang Wu

Address: College of Architecture and Urban Planning, Tongji University, Shanghai 200093, China

Email: wus@tongji.edu.cn

Corresponding Author:

Yixuan Zou

Address: China Shanghai Research Institute for Intelligent Autonomous Systems, Tongji University, Shanghai 200093, China

Email: yixuanzou@tongji.edu.cn

Fangzheng Li

Address: School of Landscape Architecture, Beijing Forestry University, Beijing 100083, China

Email: fangzhengli@bjfu.edu.cn

Jiaping Liu

a. School of Materials Science and Engineering, Southeast University, Nanjing 211189, China

b. State Key Laboratory of Engineering Materials for Major Infrastructure, Jiangsu Sobute New Materials Co., Ltd., Nanjing, China

Email:ljp@cnjsjk.cn

Zhiqiang Wu

Address: College of Architecture and Urban Planning, Tongji University, Shanghai 200093, China

Email: wus@tongji.edu.cn

Abstract

Urban areas are experiencing increasingly frequent and severe heatwaves, yet the relationship between physical heat exposure and public emotional response remains unclear. This study leveraged large language models and machine learning to investigate the divergent trajectories of the heat aggregation index (HGI) and emotional aggregation index (EGI) under three shared socioeconomic pathways.The results showed that 87.4% of cities suffered high-intensity emotional shocks, significantly exceeding the 53.5% facing severe physical exposure. This disparity revealed that underdeveloped regions faced significantly prolonged recovery periods, reflecting that physical resilience hinged on urbanization capabilities whereas emotional resilience was driven by the intensity of human-induced warming. The CMIP6 projections indicated that EGI declined about 18.2% faster than HGI over 2025–2050, widening the vulnerability gap by the 2100s. These findings demonstrated that urban resilience cannot be sustained by physical infrastructure alone and underscored the critical need to incorporate psychological adaptation into climate strategies.

Main

Propelled by the dual forces of anthropogenic climate change and urbanization, the frequency and intensity of extreme heat events globally have reached unprecedented levels[1–3]. Forecasts indicate that billions of people will be exposed to severe urban thermal environments over the coming 50 years, drastically amplifying the systemic risks to living environments[4]. Beyond the known physiological burdens, heat exposure

is intimately linked to mental health crises, ranging from rising suicide rates to a significant deterioration in subjective well-being[5]. Given these accelerating trends, the comprehensive assessment of the compound health risks to urban populations has become a critical priority in addressing the climate challenge[6,7].

While the physical dimensions of heatwaves are well-documented, quantifying their real-time psychological toll on large-scale populations remains a formidable challenge. Conventional assessments typically rely on health statistics or retrospective surveys. However these static indicators, constrained by sample sparsity and temporal lags, often fail to capture the immediate subjective discomfort and emotional fluctuations experienced by the public during extreme events[8,9]. In contrast, social media 'big data' integrated with Natural Language Processing (NLP) offers a transformative solution[10–12]. By extracting sentiment polarity and intensity from unstructured text, this approach converts expressed emotions into quantifiable, high-resolution metrics[13–15]. Crucially, such digital footprints are inherently embedded with socio-economic context, enabling the precise identification of heterogeneity and potential amplification effects across diverse demographic profiles and infrastructure distributions.

Despite effectively deconstructing disaster risk into a static superposition of hazard, exposure, and vulnerability, traditional resilience frameworks frequently fail to capture the spatiotemporal evolution of urban systems under shock[16–18]. To address this limitation, modern resilience theory emphasizes the necessity of transitioning from static snapshots to dynamic process assessments, which involves characterizing the

121 trajectory of a system deviating from its baseline by quantifying the peak intensity,
122 cumulative magnitude, and recovery time[19–21]. The subjective psychological state of the
123 public does not exist in isolation but is profoundly shaped by the intersection of local
124 environmental contexts and socio-economic conditions[22]. Even though economic
125 capital is typically viewed as a cornerstone of adaptive capacity, its ability to effectively
126 translate into a psychological buffer under the oppression of extreme heat remains
127 characterized by significant uncertainty[23,24]. Consequently, genuine urban resilience
128 hinges on synergizing the 'hard capability' of physical defense with the 'soft elasticity'
129 of social recovery.

130 This study constructed a dual-dimensional assessment framework encompassing 357
131 Chinese cities, aiming to quantify the dynamic coupling between physical heat
132 exposure and public emotional response. By integrating geo-located social sensing data
133 processed through NLP methods with high-resolution meteorological observations
134 from 2020 to 2024 (Extended Fig. 1; Supplementary Fig. 2), we derived two composite
135 metrics: the heat aggregation index (HGI) and the emotional aggregation index (EGI).
136 We initially employed Distributed Lag Non-linear Model (DLNM) to systematically
137 quantify the spatiotemporal asynchrony and lag effects of emotional feedback in
138 response to thermal exposure. To further disentangle the drivers of this dimensional
139 mismatch, we utilized interpretable machine learning methods to identify key
140 determinants and their threshold effects. Ultimately, through the integration of climate
141 change scenarios with Shared Socioeconomic Pathways (SSPs), we projected the co-
142 evolutionary trajectories of physical risk and social adaptation under three distinct

pathways: SSP1-2.6, SSP2-4.5, and SSP5-8.5. These findings provide a scientific basis for evaluating compound urban heat resilience and offer critical support for formulating precision-guided adaptation strategies.

Results

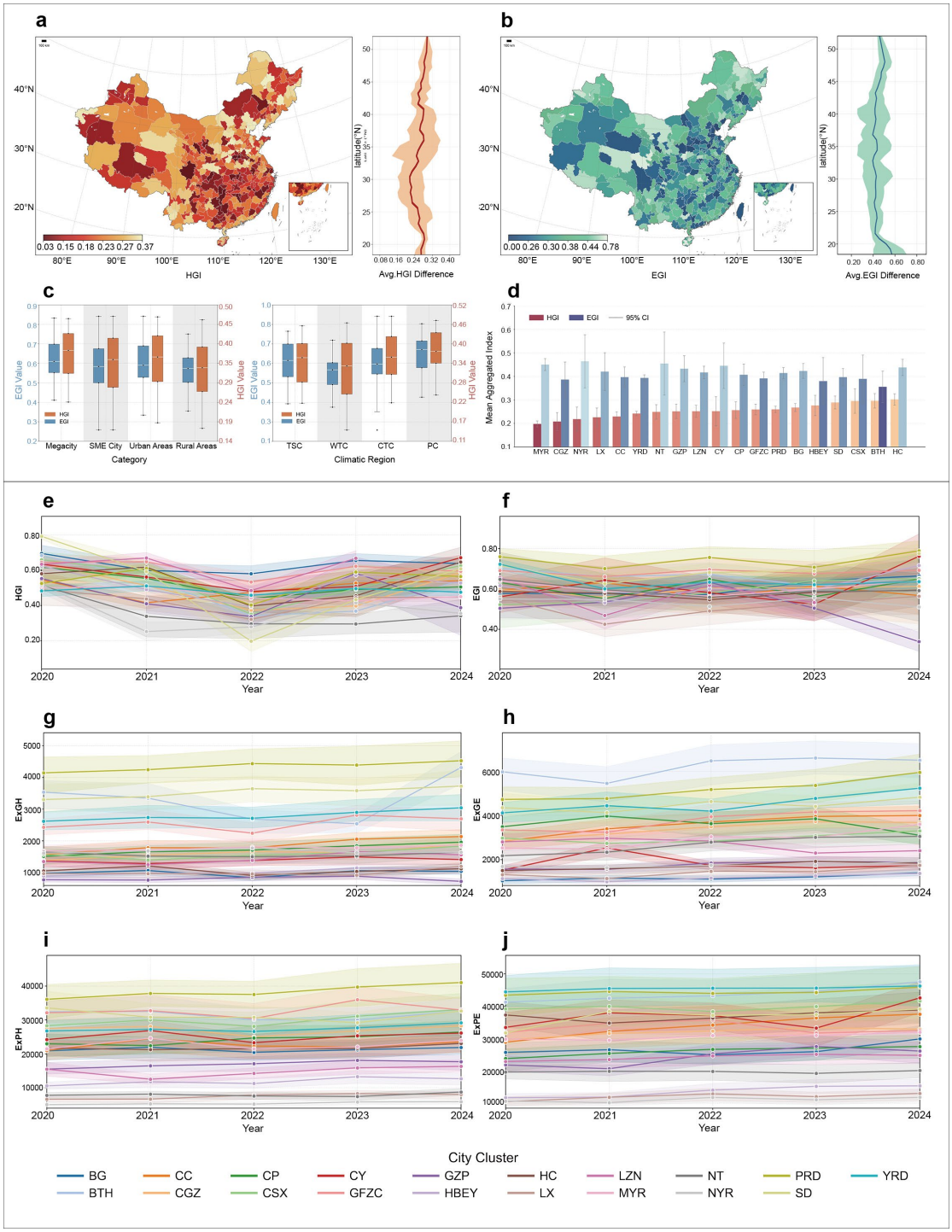
Spatial-temporal characteristics of HGI and EGI

Across 357 Chinese cities, the HGI and EGI exhibited pronounced spatial heterogeneity (Fig. 1a,b). At the national scale, the mean HGI stood at 0.253 (90% CI: 0.249–0.257), while the mean EGI reached 0.434 (90% CI: 0.427–0.441). Notably, the disparity between the lowest and highest deciles spanned approximately 103% for HGI and 98% for EGI, a gap that underscores a sharp stratification in urban capacity to physically recover from and emotionally buffer heatwaves. Latitudinal sliding-window profiles revealed a general south-to-north gradient, with cities in Northeast and North China systematically registering higher index values, whereas those in the Yangtze River basin and southern China clustered within low-to-moderate ranges. However, even within narrow 0.8° bands, the 5th–95th percentile envelope remained extensive and often approached a twofold spread. This substantial variability suggested that local attributes, such as urban form, demographic structure, and governance,can significantly modulate the resilience baseline established by broad climatic patterns.

Stratified analyses based on climatic regions settlement patterns and city clusters further unveiled these spatial differentiation characteristics (Fig. 1c–d). The plateau climate

(PC) exhibited elevated resilience baselines where mean EGI and HGI surpassed those of the warm temperate (WTC) region by approximately 20.8% (90% CI: 20.3–21.3) and 17.8% (90% CI: 17.1–18.5) respectively. Along the rural-urban gradient megacity cores demonstrated superior adaptive capacity with EGI levels exceeding rural areas by roughly 9.5% (90% CI: 8.7–10.2) and HGI by 12.2% (90% CI: 11.3–13.2). However the pronounced volatility observed in small and medium-sized cities suggests that emotional resilience does not scale linearly with urban size. At the city-cluster scale EGI in the central inland and parts of the northwestern basins surpassed that of the northern plains whereas the advantage in HGI was more concentrated within the northern and northeastern industrial belts. To clarify the mechanisms masked by the aggregated indices, HGI was decomposed into Heat Peak Severity ($IMAX_h$), Heat Recovery Time (RT_h) and Heat Cumulative Perturbation Magnitude (RP_h), and EGI into Emotion Peak Severity ($IMAX_e$), Emotion Recovery Time (RT_e) and Emotion Cumulative Perturbation Magnitude (RP_e), as defined in Methods. From an equity perspective, these disparities showed stronger inequality under socioeconomic weighting, particularly for emotional recovery time (RT_e). In contrast, the aggregated HGI and EGI appeared more evenly distributed overall.This implied that the critical gap lay not in the overall resilience levels, but in the uneven distribution of emotional recovery. Specifically, a minority of cities with high populations or GDP carried a disproportionate recovery burden, creating a clear concentration effect (Extended Fig. 2-3; Supplementary Fig. 3-4; Supplementary Notes S1–S2).

Fig. 1. Spatial patterns and temporal evolution of HGI and EGI in 357 Chinese cities from 2020 to 2024.



a,b, national mean values of HGI (a) and EGI (b) from 2020 to 2024 for 357 cities. The main panels show city-level values (darker colours indicate higher indices). The right-hand panels display latitudinal profiles constructed with a 0.8° sliding window; the solid line is the mean within each window and the shaded envelope marks the 5th–95th percentiles of city values. c Distributions of HGI (red) and EGI (teal) by climatic region and degree of urbanisation. Climatic regions are tropical–subtropical (TSC), warm temperate (WTC), cold temperate (CTC)

and plateau climate (PC); settlement types are megacity cores, small- and medium-sized cities (SME city), other urban areas and rural areas. Bar height gives the mean index for each category, black points denote the sample mean and error bars represent 90% confidence intervals across cities. d, Comparison of HGI (orange) and EGI (blue) for the 19 national city clusters: Beibu Gulf (BG), Beijing–Tianjin–Hebei (BTH), Chengdu–Chongqing (CC), Central Guizhou (CGZ), Central Plains (CP), Central Shanxi (CSX), Central Yunnan (CY), Guangdong–Fujian–Zhejiang Coastal (GFZC), Guanzhong Plain (GZP), Huhhot–Baotou–Erdos–Yulin (HBEY), Harbin–Changchun (HC), Lanzhou–Xining (LX), Liaozhongnan (LZN), Middle Yangtze River (MYR), Northern Tianshan (NT), Ningxia–Yellow River (NYR), Pearl River Delta (PRD), Shandong Peninsula (SD) and Yangtze River Delta (YRD). Bars show the mean across cities within each cluster and error bars indicate 90% confidence intervals. e,f, Annual trajectories of HGI (f) and EGI (g) for the 19 city clusters from 2020 to 2024. g,h, Annual trajectories of GDP exposure to physical heat (E_GH; g) and emotional stress (E_GE; h). i,j, Annual trajectories of population exposure to physical heat (E_PH) (i) and emotional stress (E_PE) (j). Coloured solid lines show the cluster means, filled circles mark observed yearly values and semi-transparent bands depict 90% confidence intervals obtained by bootstrapping over constituent cities.

Across the 19 major urban agglomerations (Supplementary Fig. 5), the trajectories of physical heatwaves and emotional stress decoupled significantly between 2020 and 2024. HGI dropped to its lowest point in 2022, falling 33.0% below 2020 levels. Despite recovering in 2023–2024, the 2024 average remained 11.4% below the 2020 baseline. In contrast, EGI continued to rise after 2021, increasing by 9.3% from its trough and surpassing the 2020 baseline by 1.8% in 2024. This indicates that public emotional stress intensified after a brief drop. Incorporating socioeconomic exposure metrics further widened this gap between physical recovery and growing societal burdens (Fig. 1e–j). Driven by demographic shifts and economic growth, population exposure to physical heat (E_PH) rose only moderately by 8.3% over the four years, whereas population exposure to emotional stress (E_PE) surged by 14.0%. This disparity was even more pronounced in the economic dimension: while GDP exposure to physical heat (E_GH) increased by 14.7%, the GDP exposure to emotional stress (E_GE) expanded by 18.8%. These data revealed that the burden of emotional stress on

social systems was accelerating at a rate that outpaced both the meteorological hazard itself and its physical exposure (Supplementary Fig. 6-8). Log-scale analysis attributed this widening gap to a structural divergence where HGI remained scale-neutral while EGI exhibited a distinct 'prosperity penalty' under urban expansion (Extended Fig. 4;Supplementary Note 3).

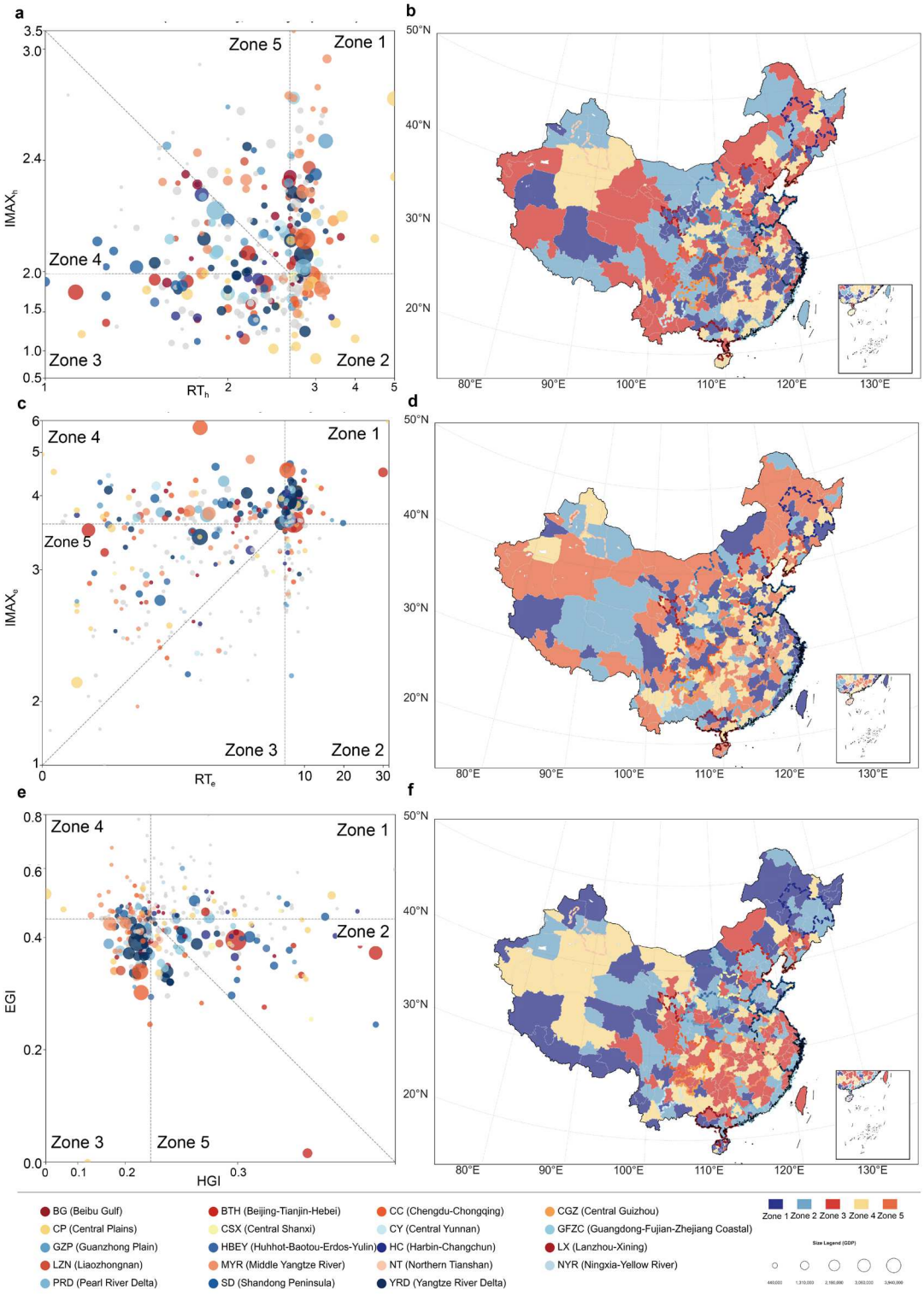
Identifying regional hotspots of socio-physical mismatch

To identify Chinese urban agglomerations requiring differentiated intervention, we investigated the interplay between physical heat exposure (RT_h, $IMAX_h$), social sentiment (RT_e, $IMAX_e$), and economic development across 357 cities (Fig. 2). The mean-thresholded pentagonal analysis showed that economic scale did not eliminate physical vulnerability; instead, GDP and physical exposure displayed a marked nonlinear relationship (Fig. 2a,b). In the physical dimension, 53.5% of cities remained in the high-impact region (Zone 1+4), and this share rose to 77.4% for basin cities in central China along the middle Yangtze River (MYR) and 73.5% for the eastern coastal Yangtze River Delta (YRD). In contrast, northern city clusters such as Beijing–Tianjin–Hebei region (BTH) benefited from geographic and climatic conditions, with roughly half of their cities located in the Zone 3. On the social side, the patterns pointed to an even stronger “emotional amplification” effect (Fig. 2c,d): 87.4% of cities experienced high-intensity emotional shocks, a pattern that was especially pronounced in YRD and eastern coast, suggesting that in highly connected and economically dynamic regions, public psychological sensitivity has already exceeded the buffering capacity of the

physical environment. Results based on population weighting showed a broadly similar spatial pattern (Supplementary Fig. 9).

A coupled assessment of the composite resilience indices (HGI and EGI) further revealed a structural mismatch between the physical and social subsystems (Fig. 2e,f). In coastal and former industrial bases such as BTH and SD, more than 55% of cities clustered in Zone 2, where physical resilience outpaced emotional resilience, forming a typical lag pattern: physical infrastructure provided a certain level of buffering, yet elevated public anxiety and gaps in social support remained evident. The most alarming signal emerged in the YRD, where 58.8% of cities clustered in Zone 3. This concentration revealed that rapid urbanization, compounded by intensified heat island effects and high social pressure, had fostered a structural resilience deficit that resisted spontaneous correction. By contrast, 93.5% of MYR cities were located in Zone 3 or Zone 4, implying that under conditions of limited physical carrying capacity, these cities relied more heavily on emotional forms of adaptation. This zonal mismatch was further supported by bivariate density analysis, which confirmed that physical and emotional resilience were not linearly coupled but instead co-modulated by distinct climatic zones and urbanization processes. (Supplementary Fig.10-12;Supplementary Note S4)

Fig. 2. Interplay of physical heat intensity, social sentiment response and aggregate resilience coupling with economic volume across Chinese cities, through a data-driven pentagonal typology.



a, c, e, Pentagonal scatter plots mapping 357 cities based on physical heat intensity (a), social sentiment fluctuation (c), and aggregate resilience coupling (e). Unlike conventional plots, the quadrant origin (dashed cross-hairs) is defined by the sample mean (X, Y) of each indicator,

representing the average performance. The quadrant with the highest data density is subdivided diagonally to form five distinct typologies (Zones 1–5). Circle sizes are scaled by urban GDP. a, Physical perspective (RT_h vs $IMAX_h$). Higher values indicate higher vulnerability. Zone 1 represents the most vulnerable 'High Intensity–Slow Recovery' type; Zone 3 represents the most resilient 'Low Intensity–Fast Recovery' type; Zone 5 denotes the dense intermediate transition type. c, Social perspective (RT_e vs $IMAX_e$). Higher values indicate higher sensitivity. Zone 1 signifies 'High Shock–Slow Recovery' (high sensitivity); Zone 3 signifies 'Low Shock–Fast Recovery' (emotional stability). e, Aggregate perspective (HGI vs. EGI). Higher values indicate stronger resilience (note the axis inversion compared to a and c). Zone 1 indicates 'Double High Resilience' (synergy); Zone 3 indicates 'Double Vulnerability' (deficit trap); Zone 2 and Zone 4 reveal 'Resilience Mismatches', representing physical-leading and emotional-leading adaptation, respectively. b, d, f, Geospatial distribution of the corresponding typologies across 19 major urban agglomerations. Map colors correspond to the zones in the scatter plots (a, c, e), and colored dashed lines delineate the boundaries of each urban agglomeration.

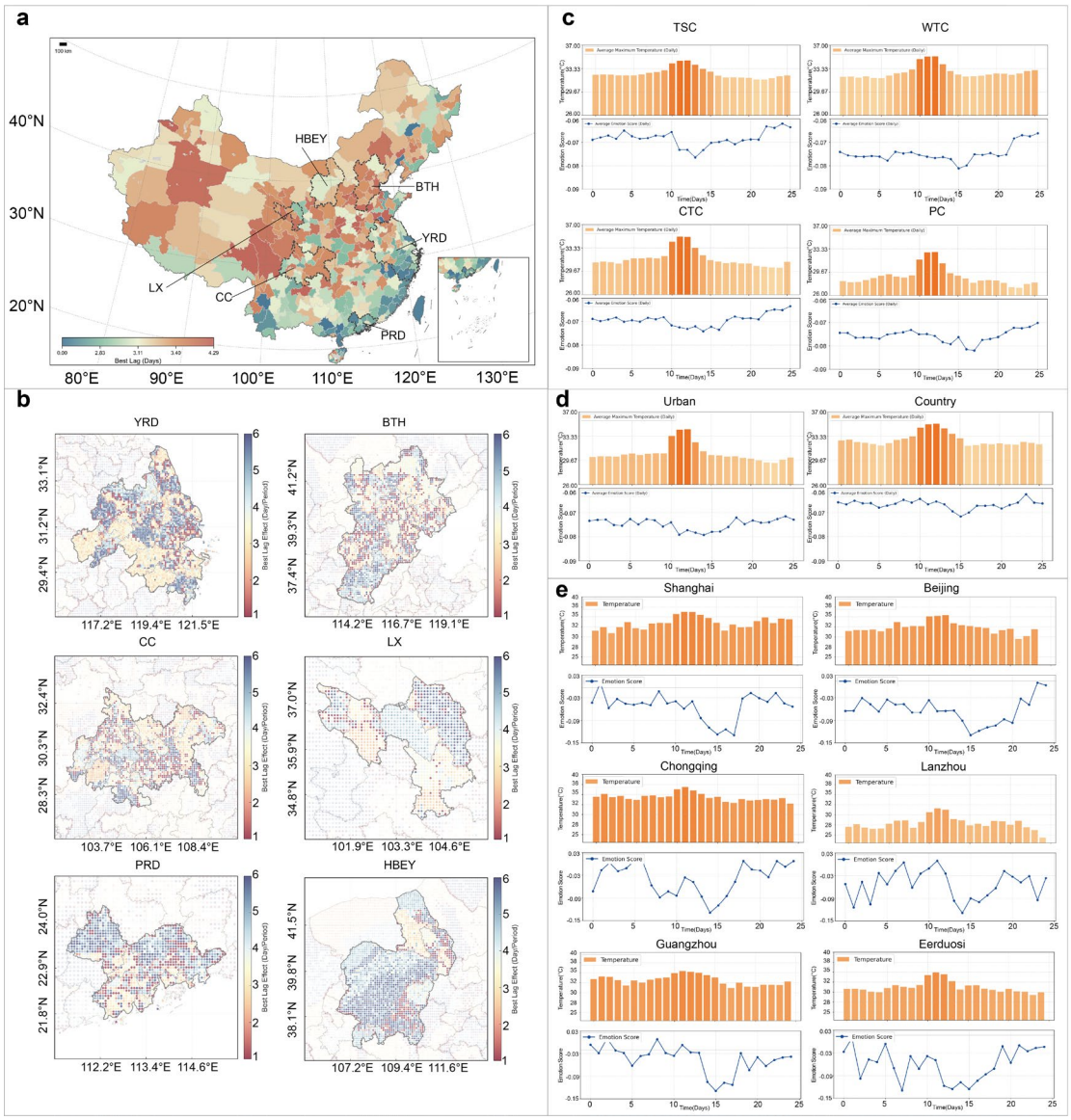
Geographic variation of lagged emotional responses to heatwaves

Estimates from the Distributed Lag Non-linear Model (DLNM) and Akaike Information Criterion (AIC) showed that the best lag day (BL) between heat exposure and emotional response increased systematically from the south-eastern coast towards the north-western inland and plateau regions (Fig. 3a; Supplementary Table 1). Coastal urbanized regions achieved a mean BL of 2 days ($P<0.001$; 90%CI: 1.9–2.1), whereas north-western inland and plateau regions reached 3.3 days ($P<0.01$; 90% CI 3.1–3.5), indicating a markedly slower response in these areas. This spatial gradient was statistically robust ($Z>1.96$, $P<0.001$). At the climate-zone scale, cities in TSC had a mean BL of 2.6 days, while those in CTC and PC reached nearly 3.2 days (Fig. 3c). In these colder and higher regions, a larger share of cities exhibited significantly negative Sen slopes ($P<0.05$), suggesting that longer lags tended to coincide with more persistent emotional deterioration. Mann–Kendall tests indicated a significant overall monotonic trend ($P<0.001$; Supplementary Fig.12). Urban areas possessed a shorter mean BL than

297 rural areas ($P<0.05$), and most urban Sen slopes were positive within the 90%
298 confidence interval, whereas rural slopes tend to remain negative, indicating faster
299 recovery in cities but longer-lasting accumulation of negative emotions in the
300 countryside (Fig. 3d).

301 After regridding simulated emotion score to 0.1°, we recalculated and averaged
302 temperature–emotion time series for representative cities from six city clusters to infer
303 BL (Fig. 3e; Supplementary Table 1; Supplementary Fig.13-15). In south-eastern
304 coastal cities (like Shanghai and Guangzhou) and the south-western basin city (like
305 Chongqing), prolonged high temperatures were associated with only modest and short-
306 lived declines in emotional scores, which rapidly returned to baseline once temperatures
307 fell. By contrast, plateau and resource-dependent inland cities (such as Lanzhou and
308 Eerduos) showed stable emotions during the early phase of the heatwave but
309 experienced sharp drops several days after the temperature peak, with BL values
310 clustering around 3–4 days ($P<0.01$). Beijing lay between these two patterns and
311 exhibits more persistent fluctuations. These findings indicated that climatic setting and
312 development pathway jointly shaped the timing and duration of societal responses to
313 heat, and they revealed a pronounced asymmetric vulnerability in psychological heat
314 resilience in northern inland and plateau regions compared with the more quickly
315 adapting coastal and basin cities (Supplementary Note S5).

Fig. 3. Spatial heterogeneity of the delay between thermal exposure and emotional response across China.



a, 5-year mean best lag day (BL) between daily maximum temperature and emotion score for all cities in China. Map colors indicate the length of the lag between heatwaves and emotional responses, from short (blue) to long (red); black lines show provincial boundaries and the inset displays island regions.b, Grid-level BL at 0.1° resolution within six representative city clusters, based on regridded emotional fields: YRD , BTH , PRD , CC , LX and HBEY . Warmer colors denote longer BL and thus slower emotional responses, whereas cooler colors indicate shorter BL.c, Superposed-epoch composites of temperature and emotion for four climate zones and for all urban versus rural grids. Panels correspond to TSC , WTC , CTC and PC ; d show all urban and rural grids, respectively. For each panel, orange bars represent the 25-day evolution of the average daily maximum temperature, and blue lines represent the corresponding average emotion score. Temperature series are calculated from daily maximum temperature, whereas

emotion scores are originally derived from 3-hourly data and then averaged to daily values for visualization.e, City-scale superposed-epoch sequences for Shanghai, Beijing, Guangzhou, Chongqing, Lanzhou and Eerduosi, obtained by averaging regridded emotion scores at 0.1° over each city.

Nonlinear determinants of HGI and EGI

Given the pronounced nonlinearity in the responses of physical and psychological heat stress, this study used an interpretable ensemble machine-learning framework that combines LightGBM with Shapley Additive exPlanations (SHAP) to build nonlinear models for both HGI, EGI and BL (Fig. 4; Extended Fig. 5;Supplementary Notes S6-8). For HGI (Fig. 4a–c), the results showed that socio-economic factors and land-cover factors contributed approximately 35.2% and 33.0% of the total feature importance, clearly exceeding urban form and geo-environmental factors (each around 16%). GDP was the most influential single predictor (29.2%), markedly higher than DEM (15.8%) and NDVI (14.1%). When GDP lay in the lower 50% of its distribution, an increase of one standard deviation was associated with an average increase of 0.018 in HGI (90% CI: 0.016–0.020), whereas in the upper 25% this effect almost vanished (90% CI: −0.002–0.003), indicating diminishing marginal benefits of economic development in high-income cities. Improvements in NDVI were likewise more effective at low levels: within the lower 50% of its distribution, a one-standard-deviation increase in NDVI raised HGI by 0.010 on average (90% CI: 0.008–0.012), but in the upper 25% the corresponding increase was only about 0.003 (90% CI: 0.001–0.004). This pattern suggests that enhancing vegetation cover substantially strengthens heat resilience in

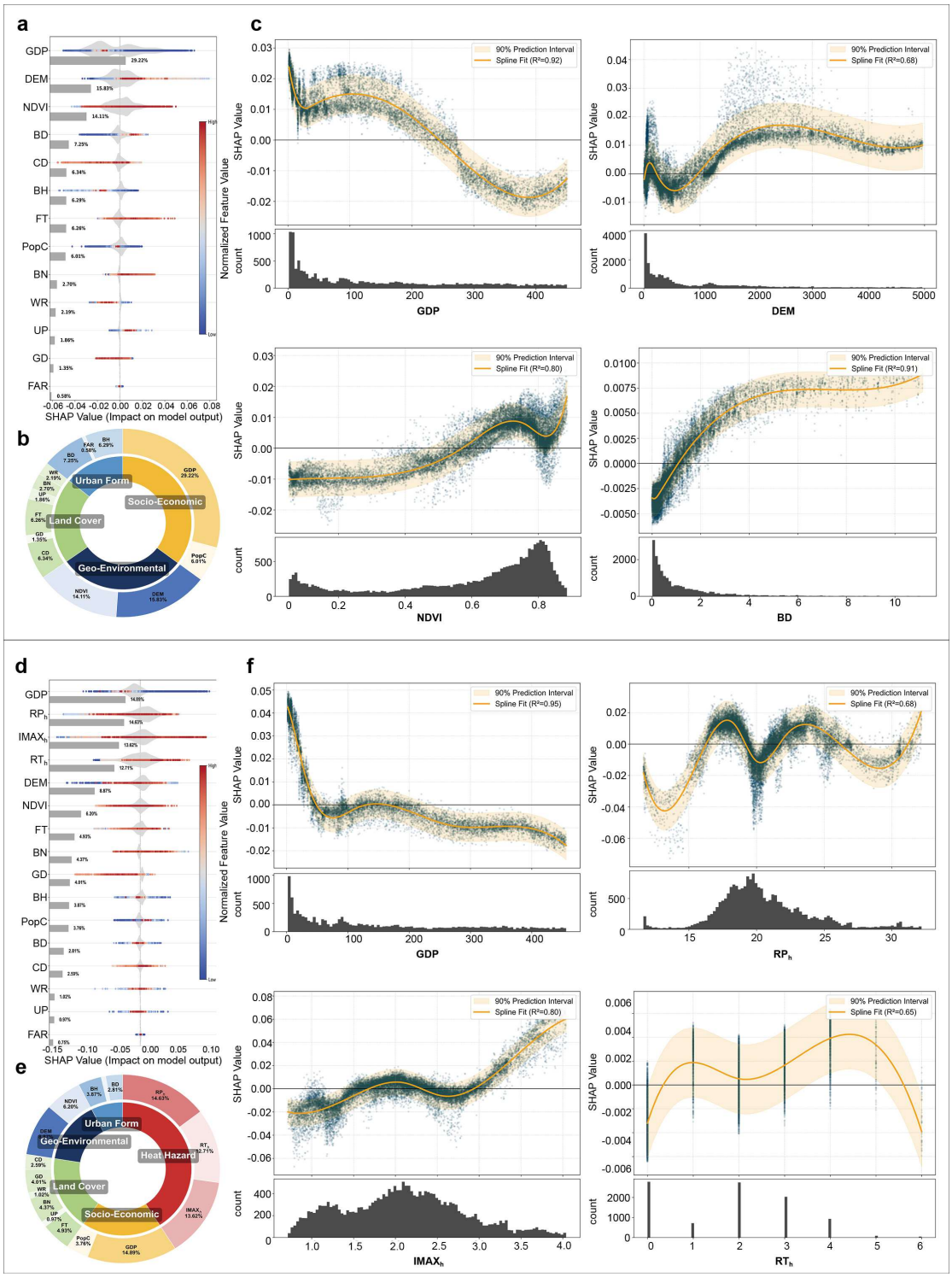
vegetation-poor cities, while additional greening yields limited gains where baseline NDVI is already high.

Building on this framework, the EGI model further incorporated $IMAX_e$, RP_e and RT_e (Fig. 4d–f). Together, these three heat-hazard variables accounted for about 40% of total feature importance, exceeding socio-economic factors (20–25%) and matching the combined contribution of land cover and urban form. EGI increased almost monotonically with $IMAX_e$: in the upper 25% of its distribution, a one-standard-deviation increase in $IMAX_e$ was associated with an average rise of 0.024 in EGI (90% CI: 0.022–0.027), whereas an equivalent increase in GDP corresponded to only 0.007 (90% CI: 0.005–0.009), indicating that event intensity played a much stronger role in amplifying emotional responses than economic conditions. The effects of RP_e and RT_e peaked around intermediate levels. When both variables were near the median of their respective distributions, a one-standard-deviation increase in RP_e and RT_e raised EGI by 0.013 (90% CI: 0.011–0.016) and 0.010 (90% CI: 0.008–0.013), respectively, while changes at the lower and upper tails were close to zero (90% CI: −0.003–0.003).

These results indicated that, compared with HGI, which was more strongly shaped by long-term structural conditions, EGI was particularly sensitive to the combination of heatwave intensity, cumulative burden and recovery rhythm, with moderate cumulative stress superimposed on high-intensity events most likely to trigger pronounced emotional peaks. Furthermore, the attribution analysis extended to the temporal dimension (Supplementary Note 8; Supplementary Fig. 16), revealing a distinct

mechanism where the BL was predominantly governed by the antagonism between physical heat intensity which tended to prolong the emotional response and economic capacity which acted to significantly compress it.

Fig. 4. The effect of each feature on HGI and EGI.



a,d, Global importance and local effect of each feature in the ensemble learning models for HGI (a) and EGI (d). In these panels, the x axis shows the SHAP value and the y axis lists the features; point colour ranges from blue to red to indicate low to high feature values. b,e, The global importance of each feature for HGI (b) and EGI (e), expressed as its mean absolute SHAP value divided by the sum over all features. c, SHAP dependence plots for GDP, DEM, NDVI and BD on HGI. f, SHAP

dependence plots for GDP, $IMAX_h$, RP_h and RT_h on EGI. In panels c and f, the x axis shows the sample feature value and the y axis shows the SHAP value (local effect on HGI or EGI); orange curves denote spline fits, shaded bands show the 90% prediction interval, and grey histograms indicate the marginal distribution of each feature, with darker point clouds representing higher sample density.

Future projections of heat resilience and exposure

Considering that Chinese cities were expected to face increasingly complex heatwave risk patterns, we used the multi-model ensemble (MME) mean of 13 CMIP6 models to project changes in EGI and HGI under the SSP1-2.6, SSP2-4.5 and SSP5-8.5 scenarios (Fig. 5a,b; Extended Fig. 6). Over 2025–2050, national mean EGI and HGI across the three scenarios decreased by about 6.5% and 5.5%, indicating that emotional resilience eroded 18.2% faster than physical defenses even in the near term. From 2050 to 2100, under SSP1-2.6 and SSP2-4.5, national mean EGI decreased by about 12% relative to 2025; however, under SSP5-8.5, it exhibited a precipitous decline, dropping to approximately 0.53. Over the same period, HGI decreased in all three scenarios, and the national mean dropped to about 0.30 under the high-emission pathway. Spatially, during 2025–2050, eastern coastal and central high-density urban agglomerations (for example, BTH, YRD and PRD) were the first to show concurrent declines in EGI and HGI (Supplementary Fig.17-18).

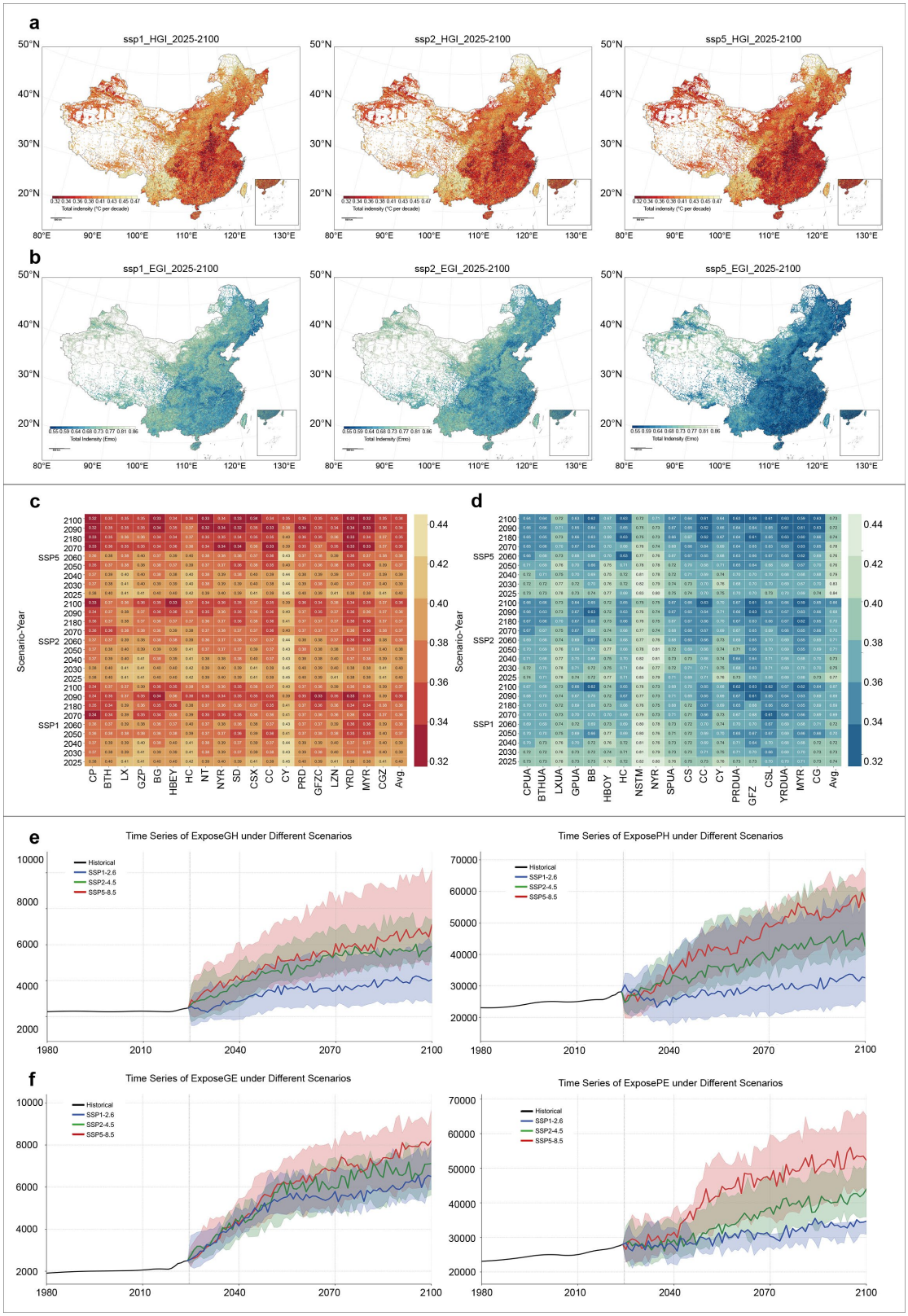
Under SSP5-8.5, these regions evolved into critical risk zones characterized by the simultaneous collapse of emotional and physical resilience during 2050–2100 (Fig. 5c,d). Critically, unlike the localized resilience observed in lower-emission scenarios, western and plateau urban agglomerations also experienced substantial erosion in EGI

alongside persistently low HGI. This shift indicated a transition from an imbalanced resilience pattern to a systemic vulnerability trap, where the historical psychological buffer was rapidly depleted under compound extreme events. Decomposing the attenuation of HGI and EGI into component drivers revealed that under the SSP5-8.5 scenario, recovery lags for heat and emotion (RT_h and RT_e) surged by 46.4%–50.1%, significantly outpacing the 25.6%–35.9% rise in peak intensity (*IMAX*). This disparity indicated that the core mechanism of resilience failure lay not in the elevation of shock peaks, but in the structural paralysis of system recovery mechanisms (Extended Fig. 7-9; Supplementary Note S9).

On this basis, Population Exposure (E_PH and E_PE), GDP Exposure (E_GH and E_GE) and Heat risk exposure ratio (R_HE) together described the combined effects of heat-risk exposure and perception bias (Fig. 5e,f; Extended Fig. 10). Between 2025 and 2100, national mean E_GH increased by about 60%, 120% and 150% under SSP1-2.6, SSP2-4.5 and SSP5-8.5. Parallel to this physical deterioration, the socio-perceived vulnerability also exhibited a substantial upward shift, as E_GE expanded by 50%, 90%, and 140% across the same scenarios. Under SSP5-8.5, for example, E_GH rose from 2.9×10^3 (90% CI: 2.0×10^3–3.8×10^3) to 7.0×10^3 (90% CI: 5.3×10^3–1.0×10^4) by the century's end, while E_GE concurrently rose from 2.7×10^3 (90% CI: 2.1×10^3–3.1×10^3) to 6.3×10^3 (90% CI: 5.7×10^3–9.3×10^3). Over the same period, R_HE increased by 20% during 2025–2050 and a further 30% rose during 2050–2100, reaching 1.27 (SSP1-2.6; 90% CI: 1.12–1.47), 1.15 (SSP2-4.5; 95% CI: 0.88–1.34) and 1.43 (SSP5-8.5; 90% CI: 1.28–1.65) by 2100. This change indicated that associated negative emotional response

intensified systematically faster than physical heat risk, especially in highly exposed eastern and central urban agglomerations under strong forcing, suggesting that adaptation strategies relying only on perception-driven spontaneous responses were likely to leave future systemic vulnerabilities to extreme heat insufficiently addressed.

Fig. 5. Future changes in heatwave resilience and socio-economic exposure under SSP1-2.6, SSP2-4.5 and SSP5-8.5 scenarios.



a,b, Spatial patterns of multi-model ensemble (MME) mean heatwave resilience index HGI (a) and

emotional resilience index EGI (b) over China, averaged for 2025–2100 under SSP1-2.6, SSP2-4.5 and SSP5-8.5. Colors show the magnitude of the indices in each grid cell, ranging from low (light) to high (dark) values, with hotter colors used for HGI and cooler blue–green colors for EGI. c,d, Decadal evolution of HGI (c) and EGI (d) for 19 major urban agglomerations from 2025 to 2100 under the three SSP–RCP scenarios. Rows denote scenario–period combinations (for example, SSP5-2100), columns denote urban agglomerations, numbers in each cell give the MME mean value, and the red–yellow (g) and blue–green (h) colour scales indicate increasing index values. e,f, National time series of exposure metrics based on HGI and predicted EGI for 1980–2100. Panels e show GDP exposure (E_GH) and population exposure (E_PH) to physical heat risk, respectively, and panels f show the corresponding exposure to emotional risk (E_GE and E_PE). Solid lines indicate the MME mean for the historical period (black) and the three future scenarios SSP1-2.6 (blue), SSP2-4.5 (green) and SSP5-8.5 (red); shaded bands of the same colors denote the intermodel spread (5th–95th percentile, approximating the 95% confidence interval). The base maps in a–f were derived from the 2019 standard map of China issued by the Ministry of Natural Resources.

Discussion

Prevailing research often conceptualizes urban climate adaptation as a linear progression from physical exposure to social response, a simplification that overlooks the structural mismatch between objective environmental limits and subjective public perception[25]. To address this gap, we utilized multi-source data across 357 Chinese cities to establish a comprehensive framework evaluating both physical (HGI) and emotional (EGI) resilience index. Coupling top-down systemic views with bottom-up public sentiments, we dissected the spatiotemporal dynamics of this composite resilience through three analytical approaches: (1) quantifying the asynchrony and lag effects between physical recovery and emotional response via DLNM models; (2) decoding non-linear drivers and threshold effects using interpretable machine learning; and (3) projecting the evolutionary trajectories and potential divergences of physical exposure versus social adaptive expectations under CMIP6 scenarios. Collectively,

these analyses offered a novel mechanistic perspective on compound urban vulnerability in a changing climate.

The divergence between physical and emotional resilience appeared to be an adaptive outcome reshaped by perception and governance layers rather than being determined solely by meteorological intensity. Public sensitivity was driven by experiential dimensions such as sustained nighttime heat and post-peak recovery, which altered the accumulation of discomfort and delayed emotional restoration despite infrastructural mitigation[9,26]. Furthermore, apparent adaptation often stemmed from short-term coping rather than the removal of physiological constraints, causing emotional fluctuations to persist across heterogeneous populations[27,28]. Social cognitive mechanisms also amplified the gap between objective protection and subjective safety, particularly in developed cities where heuristic biases and risk literacy disparities heightened sensitivity[29]. Moreover, development likely imposed a prosperity penalty where digital environments and rising safety expectations intensified the diffusion of anxiety, effectively offsetting the stabilizing benefits of physical infrastructure[30]. Consequently, engineering defenses alone proved insufficient to elevate emotional resilience, necessitating the integration of psychosocial interventions into core adaptive frameworks[31].

A key contribution of this study was quantitatively revealing the lag effect between physical heat and emotional resilience. We demonstrated that emotional stress was not synchronized with heat peaks but instead appeared with a clear delay. In general,

emotional responses in developed coastal regions resembled short-term elastic fluctuations, whereas those in northwestern inland and plateau regions exhibited systemic response delays. This divergence likely results from the interaction between geographical and social conditions. The insufficient infrastructure in these areas limits the capacity to quickly reduce heat stress through artificial means, leading to a reliance on slower natural cooling that prolongs the duration of negative emotions[32]. Furthermore, the cumulative nature of information spread suggests that immediate public attention to extreme events can persist for days, creating a lasting emotional impact[15,33]. Consequently, early warning systems must shift from focusing solely on meteorological peaks to extending psychological support into the post-heatwave recovery phase[12]. Particularly in plateau, inland, and rural hinterlands, extending psychological support into the post-peak recovery phase yields greater efficacy than confining interventions to the acute hazard onset[34,35].

Mechanistic analysis revealed that HGI and EGI did not follow the same replicable pathways. Specifically, HGI exhibited clear adaptive saturation, where the protective effects of capital accumulation and ecological improvements diminished rapidly after reaching a certain level[36]. This pattern implied that relying solely on incremental infrastructure upgrades faced a bottleneck of diminishing marginal returns. In contrast, EGI was more constrained by the characteristics of extreme events, suggesting that governance must pivot from static resource accumulation to dynamic crisis management[6,37]. Consequently, adaptation strategies required a segmented approach based on baseline levels. For underdeveloped cities, investment in economic and

ecological infrastructure remained an effective pathway to enhance resilience[38]. However, for developed cities, the focus must move beyond a reliance on physical facilities and shift toward building soft adaptation capacities. Optimizing risk communication and reshaping public safety expectations were essential to address the perceived vulnerability trap associated with high development levels[39,40].(Supplementary Note 8).

Scenario-based projections indicated a key shift in the nature of urban heat risk. Risk no longer rose only through a gradual warming background. Development also locked people and assets back into high-risk areas. Even as physical hazards continued to intensify, population exposure and GDP exposure by 2100 were still expected to rise by about 130% and 150%, respectively. This pattern suggested that location advantages and investment returns often steered new growth along existing development paths into high-risk zones, making rising exposure harder to reverse[41–43]. At the same time, delayed public recognition of risk allowed hazards to accumulate without being noticed. Once future extremes exceeded design levels set by historical maxima, underlying vulnerability would surface through surging electricity and cooling demand and cascading failures of critical infrastructure, turning heat risk from a single-event issue into a persistent pressure on urban stability[44,45]. Governance therefore needed to move upstream from after-the-fact response to development decisions, embed heat risk into planning and investment choices, and use stress tests and key system upgrades, such as strengthening power-grid resilience and cooling provision, to reduce the destabilising effects of simultaneous growth in hazard and exposure[46,47].

We acknowledged certain limitations inherent in this study. Primarily, the construction of EGI relied heavily on social media data, which was inevitably subject to digital demographic biases. This reliance potentially skewed sensitivity towards the emotional fluctuations of younger urban cohorts while underrepresenting the psychological distress of elderly and rural populations. Furthermore, although the study period afforded daily-scale observations, this relatively temporal span limited the capture of long-term social adaptive processes. Additionally, future scenario projections were predicated on the assumption of stationarity in historical relationships. However, potential transformations in social institutions or climate adaptation policies could trigger non-linear systemic shifts.

In conclusion, by constructing a dual-dimensional assessment framework, this study revealed the critical divergence between physical heat exposure and public emotional response. We found that emotional recovery was not synchronized with physical mitigation but was instead shaped by regional development levels and cognitive differences. Future projections also warned that economic growth or spontaneous adaptation alone could not reverse the continued rise in high-risk exposure. Consequently, the results indicated that governance needed to move from reactive coping to proactive planning, positioning psychosocial adaptive capacity at the core to minimize the silent accumulation of vulnerability.

Methods

Data

Emotion data

Leveraging a Python-based crawler interfaced with the Sina Weibo streaming API, we curated a dataset of 11 million geolocated comments spanning the period from 2020 to 2024. To precisely capture public sentiment regarding heatwaves, the corpus was filtered using a targeted keyword strategy, identifying texts containing terms such as 'hot,' 'high temperature,' 'heatstroke,' and 'stifling.' Each retained record preserved critical spatiotemporal attributes, specifically the text content, geographic coordinates, and publication timestamp[48].

Historical meteorological data

To characterize the long-term meteorological context, we employed the ECMWF ERA5-Land reanalysis dataset to retrieve hourly climate variables at a 0.1° spatial resolution. Meteorological series were extracted by identifying the grid cell nearest to the centroid of each target mesh, after which we computed the daily maximum (Tmax), minimum (Tmin), and mean temperatures for each unit across the 1980–2024 study period. Finally, city-specific thermal profiles were synthesized by calculating the spatially weighted average of all grid cells encompassed within the respective urban boundaries.

Future meteorological data

Projected daily maximum (T_{max}) and minimum (T_{min}) temperature series were synthesized using Global Climate Model (GCM) simulations from the Coupled Model Intercomparison Project Phase 6 (CMIP6). This archive included historical runs driven by all forcing (ALL), greenhouse gas (GHG), and natural (NAT) vectors[1,7]. To ensure robustness, we restricted our ensemble to GCMs providing a minimum of three members per forcing experiment, yielding a final subset of 13 validated models (Supplementary Table 3). Following established protocols, future risks were assessed under three distinct Shared Socioeconomic Pathways (SSP1-2.6, SSP2-4.5 and SSP5-8.5), characterizing a spectrum of futures from stringent carbon control to intermediate mitigation and unconstrained emissions[42,43].

Population and GDP data

Spatially explicit population projections for China were retrieved from the Spatial Population Scenarios database (www.cgd.ucar.edu/iam/modeling/spatial-population-scenarios.html), providing 1 km × 1 km gridded data spanning historical (2010–2024) and future (2025–2100) horizons under three SSPs. City-level demographic aggregates were derived by summing the constituent grid cells within each urban boundary. To capture parallel economic trajectories, we acquired historical and projected gridded GDP datasets from WorldPop (https://hub.worldpop.org). These economic layers, harmonized with the selected SSP scenarios, were similarly integrated and aggregated to the municipal unit to ensure consistency across the socioeconomic exposure assessment.

Auxiliary datasets

Auxiliary datasets included Global Urban Boundaries (GUB), elevation, land cover types, and built environment data. The 2018 GUB data were utilized to delineate urban and rural areas, while the 1-km Köppen-Geiger climate classification defined China's major climatic zones. Topographic data, comprising elevation and slope, were provided by the Resource and Environment Science and Data Center (https://www.resdc.cn). Land cover data were collected based on the China Land Cover Dataset (CLCD) with a spatial resolution of 30 m. The Normalized Difference Vegetation Index (NDVI) dataset was derived from MOD13A3 satellite products and downloaded from the EOSDIS website at a 1 km × 1 km resolution. For urban built environment metrics, this study utilized the Global Human Settlement Layer (GHSL) dataset (https://ghsl.jrc.ec.europa.eu/) to calculate intra-urban metrics for grid cells, which were then aggregated to the city level via weighted averaging. These indicators included Building Density (BD), Building Height (BH), and Floor Area Ratio (FAR), see details in Supplementary Table 2 and Supplementary Note 6.

Statistical analysis

Definitions of heatwaves

Identification of heatwave events relies on the synthesized T_{max} series, utilizing an adaptive compound threshold framework. Relative to the 1980–2014 baseline, we established a dual-criterion system: an absolute threshold (T_{abs}) fixed at 35°C, reflecting human physiological tolerance and China Meteorological Administration (CMA) standards, and a relative threshold (T_{rel}) defined as the 95th percentile within a

15-day moving window to filter seasonal background noise. Addressing China's significant climatic heterogeneity, the determination logic remains spatially adaptive. For most urban areas, heatwave days are classified by the simultaneous satisfaction of both criteria ($T_{max} \geq T_{abs} \cap T_{max} > T_{rel}$). In contrast, for high-latitude or cold-region cities where summer extremes seldom reach 35°C, the protocol applies only the relative threshold, ensuring the capture of statistically significant warming anomalies specific to those local climates.

A discrete heatwave event was defined by the persistence of daily maximum temperatures meeting the aforementioned criteria for at least three consecutive days[1]. Within the 2020 to 2024 study period, the protocol permitted the identification of multiple non-overlapping events within a single city for any given year. Each event i was anchored by its onset date $D_{start}(i)$, which formed the basis for a standardized sliding window of 25 days, denoted as $W_{\text{seq}}(i) = [D_{\text{start}}(i) - 10, D_{\text{start}}(i) + 14]$. This temporal sequence explicitly incorporated a 10-day precursor phase, designed to capture the synoptic-scale accumulation of atmospheric circulation processes prior to the thermal outbreak. Ultimately, the systematic extraction of corresponding spatiotemporal raster series established a standardized database of 5,453 independent samples, serving as the empirical foundation for quantifying the underlying physical mechanisms and social impacts (Extended Fig. 1; Supplementary Fig. 2).

Processing of Sentiment Time Series

To assess public psychological responses during heatwaves, 11 million geotagged Weibo comments were spatially and temporally aligned with the standardized heatwave

event windows (W_{seq}). In the sentiment quantification phase, we employed the HFL-Chinese-BERT deep learning model, which optimizes Chinese semantic understanding by leveraging whole word masking strategies, thereby outperforming standard BERT architectures in sentiment classification tasks[49]. Following fine-tuning, the model generated probability distributions for positive (P_{pos}), neutral (P_{neu}), and negative (P_{neg}) categories for each comment. On this basis, we defined a continuous sentiment score $S(p)$ on the interval [-1, 1], calculated as $S(p) = P_{pos} - P_{neg}$. This formulation effectively transformed unstructured textual data into high-fidelity emotional valence metrics, enabling precise quantification of public sentiment dynamics (Extended Fig. 1; Supplementary Fig. 2).

The construction of city-level daily sentiment time series served to characterize the collective emotional fluctuations throughout heatwave episodes. For each day t encompassed by the standardized window W_{seq}, the analysis aggregated the full ensemble of comments geolocated within the urban perimeter. This spatial integration allowed for the computation of the city-wide daily mean sentiment score:

$$S_{city}(c,t) = \frac{1}{|P(c,t)|} \sum_{p \in P(c,t)} S(p) \quad (1)$$

A 0.1° resolution grid analysis framework was established to unveil intra-urban emotional heterogeneity and convert discrete social media points into continuous spatial surfaces. In response to the inherent spatial irregularity and sparsity of the dataset, the procedure initially computed sentiment means for individual grid units before applying Ordinary Kriging. This interpolation technique leveraged the semivariogram to model spatial autocorrelation, thereby providing the Best Linear

Unbiased Estimate (BLUE) for unobserved areas. Ultimately, the chronological stacking of these generated daily continuous surfaces formed a corresponding 25-day sentiment raster sequence for each heatwave event, achieving precise spatiotemporal alignment between physical heat exposure and social emotional response at the pixel scale.

Definitions of HGI and EGI

Resilience is conceptually defined as the capacity of a system to minimize functional degradation and accelerate recovery following anomalous perturbations[50]. Given the inherent non-stationarity of urban thermal environments and public sentiment time series, traditional static baseline methods often fail to disentangle long-term climatic trends from short-term abrupt disturbances[51]. Consequently, the analysis incorporated Fast Fourier Transform (FFT) as the core mechanism for signal decoupling. The procedure initially transformed raw time series from the time domain to the frequency domain, where a low-pass filter truncated high-frequency components. A subsequent inverse transformation reconstructed a dynamic baseline (X_{trend}), representing the system's routine equilibrium dynamics. Subtracting the baseline clearly isolated the unusual changes. Based on this zero-mean residual series, three critical resilience metrics were derived: (1) Peak Severity ($IMAX_t$), the maximum deviation amplitude, quantifying impact intensity; (2) Recovery Time (RT_t), the duration required for the system to revert from the peak to a dynamic equilibrium state; and (3) Cumulative Perturbation Magnitude (RP_t), the area under the anomaly curve (AUC), characterizing the aggregate excess load borne by the system throughout the event cycle.

To comprehensively assess systemic resilience, we constructed the physical resilience index (HGI) and the emotional resilience index (EGI).These composite indices were derived from the three aforementioned monomeric metrics ($IMAX_t$, RT_t, RP_t), representing the physical and emotional dimensions, respectively. Acknowledging that simple linear weighting often fails to capture the constraining relationships among resilience components, the study proposed a Hybrid Compensatory & Non-compensatory Model. Specifically, the Max-normalization Inversion technique converted all 'cost-type' indicators into 'benefit-type' performance scores within the [0, 1] interval, where 1 signifies optimal resilience and 0 indicates total failure. The general formulation for the composite index is given by:

$$Agg_{index}^{t} = \alpha \underbrace{\left(1 - \frac{RT_t}{RT_{t,\max}}\right)}_{\text{Rapidity}} + (1-\alpha) \underbrace{\left[\left(1 - \frac{IMAX_t}{IMAX_{t,\max}}\right) \times \left(1 - \frac{RP_t}{RP_{t,\max}}\right)\right]}_{\text{Resistance}} \quad (2)$$

This hybrid model (weighting factor fixed at 0.333) deconstructed systemic resilience into two orthogonal dimensions: Rapidity and Resistance. The linear component of the equation characterized Rapidity, permitting linear compensation between scores. In contrast, the multiplicative term encapsulated Resistance and absorptive capacity, where extreme failure in either $IMAX_t$ or RP_t resulted in the total nullification of the resistance function. This non-compensatory mechanism effectively prevented scenarios of rapid recovery despite catastrophic structural damage from being erroneously classified as high resilience, ensuring that the HGI and EGI indices faithfully reflected the comprehensive capabilities of physical and social systems under extreme stress.

AIC-Optimized DLNM Construction and Temporal Feature Extraction

To precisely elucidate the delayed effects and non-linear characteristics of heatwave

impacts on public sentiment, the study employed a Distributed Lag Non-linear Model (DLNM). Unlike traditional linear approaches that assume immediate impacts, the DLNM uses a cross-basis function to fit a two-dimensional surface that simultaneously captures both the temperature-sentiment relationship and the time lag patterns[52]. Addressing the potential fitting biases inherent in fixed lag lengths, we implemented an adaptive lag optimization algorithm grounded in the Akaike Information Criterion (AIC). For each spatial unit, a spectrum of candidate models with maximum lags ranging from 0 to 7 days was iteratively constructed; the model exhibiting the minimum AIC was subsequently selected as the optimal explanatory framework. The core equation and cross-basis function were defined as follows:

$$Y_t = \alpha + s(x_t, \text{lag}; \eta) + \gamma \mathbf{Z}_t + \varepsilon_t \quad (3)$$

$$s(x_t, \text{lag}; \eta) = \sum_{j=1}^{v_x} \sum_{k=1}^{v_l} \eta_{jk} \cdot \left(\phi_j(x_t) \times \psi_k(\text{lag}) \right) \quad (4)$$

Where Y_t denoted the sentiment score at time *t*, α represented the model intercept, and $s(x_t, \text{lag}; \eta)$served as the cross-basis function. This function was constituted by a bi-linear combination of basis functions for two dimensions: the heat exposure dimension, $\phi_j(x_t)$, modeled via quadratic splines; and the lag dimension, $\psi_k(\text{lag})$, modeled via natural splines. Furthermore, $\mathbf{Z}_t$ signified the vector of control covariates, γ denoted the corresponding coefficient vector, and ε_t accounted for the model residuals. Through an AIC minimization screening process, the optimal lag period parameter (BL) was definitively identified for each spatial unit.

Following the identification of the optimal lag structure and the temporal parameter (BL), the Slicing & Reduction operation was executed to quantify specific heatwave

impact characteristics. This procedure collapsed the complex three-dimensional 'exposure-lag-response' surface into a one-dimensional curve along the lag dimension. Such reduction intuitively characterized the dynamic deviation trajectory of sentiment valence relative to the baseline state (typically the optimum temperature) throughout the interval from 0 to BL days following extreme heat stress. Specifically, the heat exposure variable was fixed at the city-specific extreme high-temperature threshold (x_t=T_{ext}), thereby extracting a conditional response function with respect to lag days from the cross-basis matrix. The mathematical formulation for the sliced effect curve is expressed as:

$$\beta(l \mid T_{ext}) = \sum_{k=1}^{v_l} \eta k \cdot \psi kl \tag{5}$$

Where, $\beta(l \mid T_{ext})$ denoted the marginal deviation of public sentiment scores relative to the baseline state on day *l* following the onset of an extreme heat event. Furthermore, $\psi_k(l)$ corresponded to the natural spline basis functions along the lag dimension, while $\tilde{\eta}_k$ signified the linear coefficient vector, recombined subsequent to fixing the temperature dimension. Predicated on this derived one-dimensional response curve, the three aforementioned core resilience metrics were formally defined as functions of the curve's morphological characteristics:

$$IMAX_t = \max_{l\in[0,BL]} |\beta(l \mid T_{\text{ext}})| \tag{6}$$

$$RT_t = \min\{l > PL \mid \beta(l \mid T_{\text{ext}}) \approx 0\} - PL \tag{7}$$

$$RP_t = \sum_{l=0}^{BL} \beta(l \mid T_{\text{ext}}) \tag{8}$$

Empirical modeling

An interpretable machine learning framework integrating LightGBM and SHAP was constructed to deconstruct the non-linear mechanisms driving the composite resilience of physical heat and emotional response. Acknowledging the susceptibility of single-training models to data noise and parameter sensitivity, the analysis incorporated Monte Carlo Simulation (MCS) to significantly enhance model robustness. Specifically, the protocol involved the execution of 100 independent stochastic trials, wherein Bayesian Optimization was employed to adaptively search for optimal hyper-parameters during each iteration, thereby ensuring maximal generalization performance across varying stochastic distributions[53]. Building on this ensemble, the SHAP (Shapley Additive Explanations) algorithm facilitated a posterior analysis of the MCS-generated models, quantifying the marginal contribution of various urban elements to resilience through a game-theoretic lens. Furthermore, independent cross-validations were rigorously conducted across 19 major urban agglomerations in China (results detailed in Extended Data Fig. 5 and Supplementary Notes S7), which confirmed the statistical soundness of the attribution findings.

Extreme heat exposure indexes

To quantify the superimposed effects of heat risk through a coupled 'physical-social' lens, an exposure and perception bias metric framework was established, anchored in population (POP) and economic (GDP) carriers. Within this framework, the physical heat risk exposure indices (E_GH and E_PH) measured the socio-economic load sustained by the system per unit of HGI. Given the characterization of HGI as a positive safety indicator, the formulation positioned it as the denominator to derive a positive

765 exposure metric, calculated as follows:

766 $$E_PH = \frac{\mathrm{POP}}{H_AGG + \epsilon}, E_GH = \frac{\mathrm{GDP}}{H_AGG + \epsilon} \quad (9)$$

767 Correspondingly, the emotional vulnerability exposure indices (E_GE and E_PE)
768 utilized EGI to quantify the socio-economic burden sustained per unit of emotional
769 carrying capacity. The computation was governed by the following formula:

770 $$E_PE = \frac{\mathrm{POP}}{E_AGG + \epsilon}, E_GE = \frac{\mathrm{GDP}}{E_AGG + \epsilon} \quad (10)$$

771 Finally, to discern the asynchrony between physical environmental conditions and
772 public responses, the Physical-Emotional Bias Ratio (R_HE) was constructed. This
773 metric facilitated a direct juxtaposition of physical safety standards against socially
774 perceived resilience:

775 $$R_HE = \frac{H_AGG}{E_AGG + \epsilon} \quad (11)$$

776 **Spatiotemporal Equity and Local Heterogeneity Analysis**

777 A multi-scale equity assessment framework encompassing both macro and micro
778 dimensions was established. At the macro level, Gini Coefficients for HGI, EGI, and
779 their sub-indicators were computed, weighted specifically by POP , GDP, and
780 geographic area (Area), alongside the construction of Lorenz Curves. Quantification of
781 the curve's deviation from the line of equality characterized the concentration effects of
782 resource allocation or risk burdens within specific demographic groups and spatial
783 domains. Conversely, at the micro scale, to capture localized spatial polarization, the
784 Local Disparity Index was introduced. By calculating the absolute deviation between
785 each grid unit and the mean of its topological neighbors, this metric identified distinct
786 'inequality highlands' or 'depressions' that were significantly decoupled from their

surrounding environments.

Sensitivity and Robustness Analyses

For the assessment of GCM, the study selected a suite of 13 models from the CMIP6, including CanESM5, EC-Earth3, FGOALS-g3, GFDL-CM4, INM-CM4-0, INM-CM5-0, IPSL-CM6A-LR, KACE-1-0-G, MPI-ESM1-2-HR, MRI-ESM2-0, NorESM2-LM, NorESM2-MM, and TaiESM1 (Supplementary Table 3). Using the ECMWF ERA5-Land reanalysis dataset as the observational benchmark, a Taylor Diagram facilitated a multi-dimensional performance assessment of each model (Extended Fig.4). This diagrammatic approach synthesized three key metrics—correlation coefficient (CC), centered root-mean-square difference (RMSD), and standard deviation (SD)—within a polar coordinate system, while a non-parametric Wilcoxon test determined the statistical significance of differences. Following this evaluation, the Equidistant Cumulative Distribution Function (EDCDF) method corrected biases in the raw temperature data, which were subsequently downscaled to a 0.1° grid via bilinear interpolation. Ultimately, this Multi-Model Ensemble (MME) approach effectively mitigated the systematic biases inherent in individual GCMs, thereby significantly enhancing the physical robustness of future extreme heat exposure projections.

To validate the sensitivity of social media data to temporal granularity, the Mann-Kendall (MK) trend test was utilized to contrast serial characteristics across all cities under varying temporal resolutions (Supplementary Fig.12; Supplementary Table 1). The analysis revealed that trends at the 3-hour resolution demonstrated the highest statistical significance, with p-values consistently falling below 0.05 (satisfying the 95%

809 confidence criterion). Consequently, a 3-hour temporal granularity was adopted for all
810 sentiment series in the subsequent computation of resilience indices (See details in
811 Supplementary Notes S5).
812 To mitigate potential interpretability biases arising from feature redundancy, a dual-
813 diagnostic approach employing Variance Inflation Factor (VIF) and Pearson correlation
814 coefficients was implemented. Variables exhibiting high multicollinearity were
815 systematically excluded based on strict thresholds: a VIF value exceeding 5 or an
816 absolute Pearson correlation coefficient (|r|) surpassing 0.8 (Supplementary Fig.19).
817 A local sensitivity analysis was conducted to assess the impact of minor perturbations
818 in input features on LightGBM model outputs. Specifically, the Finite Difference
819 Method (FDM) approximated the numerical partial derivatives of the model output with
820 respect to each input parameter. The standard deviation of each feature was selected as
821 the specific perturbation magnitude, thereby ensuring that these perturbations reflected
822 the natural variability inherent in the dataset. The calculation of these numerical partial
823 derivatives was governed by the following formulation:
824 $$S_{i,p} = \frac{f(x_{i,p} + \sigma_p) - f(x_{i,p})}{\sigma_p} \quad (12)$$
825 Where, f denoted the trained LightGBM model, $x_{i,p}$ signified the raw value of the p-th
826 feature for the i-th sample, and σ_p corresponded to the standard deviation of that feature.
827 By introducing minor perturbations within the scope of natural variation and
828 monitoring the resultant output shift $f(x_{i,p} + \sigma_p) - f(x_{i,p})$, the model's local
829 sensitivity to specific features was quantified, thereby ensuring predictive stability
830 under natural feature fluctuations.

Data Availability

Data used in this study are collected from the following sources: Sina Weibo Open Platform, https://open.weibo.com/; ECMWF ERA5-Land reanalysis, https://cds.climate.copernicus.eu/; CMIP6 GCM simulations, https://esgf-node.llnl.gov/projects/cmip6/; Spatial Population Scenarios, https://www.cgd.ucar.edu/iam/modeling/spatial-population-scenarios.html; WorldPop, https://hub.worldpop.org; Resource and Environment Science and Data Center, https://www.resdc.cn; China Land Cover Dataset (CLCD), https://doi.org/10.5281/zenodo.4417810; Global Urban Boundaries (GUB), http://data.ess.tsinghua.edu.cn; Köppen-Geiger Climate Classification, http://www.gloh2o.org/koppen/; MOD13A3 NDVI, https://lpdaac.usgs.gov/; Global Human Settlement Layer (GHS-DUC), https://human-settlement.emergency.copernicus.eu/ghs_duc2023.php; Global WaterPack, https://doi.org/10.15489/VCALR2S1QV66; Nighttime Light (NTL), https://dataverse.harvard.edu/dataset.xhtml?persistentId=doi:10.7910/DVN/YGIVCD; SRTM, https://www.earthdata.nasa.gov/sensors/srtm; Land Surface Temperature, https://doi.org/10.25380/iastate.c.5078492.v3.

Acknowledgements

The research was funded by the National Natural Science Foundation of China [grant number: 52508078]; the Shanghai Natural Science Foundation Project [grant number:

25ZR1402513]; National Natural Science Foundation of China [grant number: 52522801]

Reference

1. Liao, S. *et al.* Temperature-related hospitalization burden under climate change. *Nature* **644**, 960–968 (2025).
2. Manoli, G. *et al.* Magnitude of urban heat islands largely explained by climate and population. *Nature* **573**, 55–60 (2019).
3. Krayenhoff, E. S., Moustaoui, M., Broadbent, A. M., Gupta, V. & Georgescu, M. Diurnal interaction between urban expansion, climate change and adaptation in US cities. *Nature Clim Change* **8**, 1097–1103 (2018).
4. Wang, J. *et al.* Anthropogenic emissions and urbanization increase risk of compound hot extremes in cities. *Nat. Clim. Chang.* **11**, 1084–1089 (2021).
5. Burke, M. *et al.* Higher temperatures increase suicide rates in the United States and Mexico. *Nature Clim Change* **8**, 723–729 (2018).
6. Raymond, C. *et al.* Understanding and managing connected extreme events. *Nat. Clim. Chang.* **10**, 611–621 (2020).
7. Liu, J. *et al.* Rising cause-specific mortality risk and burden of compound heatwaves amid climate change. *Nat. Clim. Chang.* **14**, 1201–1209 (2024).
8. Xue, T., Zhu, T., Zheng, Y. & Zhang, Q. Declines in mental health associated with air pollution and temperature variability in China. *Nat Commun* **10**, 2165 (2019).
9. Moore, F. C., Obradovich, N., Lehner, F. & Baylis, P. Rapidly declining remarkability of

872 temperature anomalies may obscure public perception of climate change. *Proceedings of the*
873 *National Academy of Sciences* **116**, 4905–4910 (2019).
874 10.Lee, T.-H. *et al.* Arousal increases neural gain via the locus coeruleus–noradrenaline system in
875 younger adults but not in older adults. *Nat Hum Behav* **2**, 356–366 (2018).
876 11.Cheng, Y. *et al.* Climatic and Economic Background Determine the Disparities in Urbanites'
877 Expressed Happiness during the Summer Heat. *Environmental Science & Technology*
878 https://doi.org/10.1021/acs.est.3c01765 (2023) doi:10.1021/acs.est.3c01765.
879 12.Dou, M. *et al.* Public responses to heatwaves in Chinese cities: A social media-based geospatial
880 modelling approach. *International Journal of Applied Earth Observation and Geoinformation*
881 **134**, 104205 (2024).
882 13.Hua, Y., Qiu, Y. & Tan, X. The effects of temperature on mental health: evidence from China. *J*
883 *Popul Econ* **36**, 1293–1332 (2023).
884 14.Kramer, A. D. I., Guillory, J. E. & Hancock, J. T. Experimental evidence of massive-scale
885 emotional contagion through social networks. *Proceedings of the National Academy of Sciences*
886 **111**, 8788–8790 (2014).
887 15.Huang, X. *et al.* Social media mining under the COVID-19 context: Progress, challenges, and
888 opportunities. *International Journal of Applied Earth Observation and Geoinformation* **113**,
889 102967 (2022).
890 16.Lei, Y., Cao, H., Zhou, X., Mills, J. & Xiao, W. Impact of Land Use/Land Cover Changes on
891 Urban Flooding: A Case Study of the Greater Bay Area, China. *IEEE Journal of Selected Topics*
892 *in Applied Earth Observations and Remote Sensing* **17**, 13261–13275 (2024).
893 17.Chen, S. *et al.* Long-term impacts of heatwaves on accelerated ageing. *Nat. Clim. Chang.* **15**,

1000–1007 (2025).

18. Huang, S. *et al.* Widespread global exacerbation of extreme drought induced by urbanization. *Nat Cities* **1**, 597–609 (2024).

19. Boulton, C. A., Lenton, T. M. & Boers, N. Pronounced loss of Amazon rainforest resilience since the early 2000s. *Nat. Clim. Chang.* **12**, 271–278 (2022).

20. Zhou, S. *et al.* Towards climate-adaptive equality in coastal megacities: Assessing urban flooding risk disparities and nonlinear effect of multidimensional indicators through an interpretable LightGBM-SHAP framework. *Sustainable Cities and Society* **132**, 106809 (2025).

21. Boulton, C. A., Lenton, T. M. & Boers, N. Pronounced loss of Amazon rainforest resilience since the early 2000s. *Nat. Clim. Chang.* **12**, 271–278 (2022).

22. Rupp, R. F., Vásquez, N. G. & Lamberts, R. A review of human thermal comfort in the built environment. *Energy and Buildings* **105**, 178–205 (2015).

23. Gao, S. *et al.* Urbanization-induced warming amplifies population exposure to compound heatwaves but narrows exposure inequality between global North and South cities. *npj Clim Atmos Sci* **7**, 154 (2024).

24. Tripathy, K. P., Mukherjee, S., Mishra, A. K., Mann, M. E. & Williams, A. P. Climate change will accelerate the high-end risk of compound drought and heatwave events. *Proceedings of the National Academy of Sciences* **120**, e2219825120 (2023).

25. Onoda, S. Identifying daily life vulnerability and regional homeostasis: verbalising homeostasis landscape in regional policy for disaster areas of Tohoku, Japan. *npj Urban Sustain* **5**, 10 (2025).

26. Howe, P. D., Marlon, J. R., Wang, X. & Leiserowitz, A. Public perceptions of the health risks of extreme heat across US states, counties, and neighborhoods. *Proceedings of the National*

916 *Academy of Sciences* **116**, 6743–6748 (2019).

917 27.Minor, K., Bjerre-Nielsen, A., Jonasdottir, S. S., Lehmann, S. & Obradovich, N. Rising
918 temperatures erode human sleep globally. *One Earth* **5**, 534–549 (2022).

919 28.Obradovich, N., Migliorini, R., Mednick, S. C. & Fowler, J. H. Nighttime temperature and
920 human sleep loss in a changing climate. *Science Advances* **3**, e1601555 (2017).

921 29.Raymond, C., Matthews, T. & Horton, R. M. The emergence of heat and humidity too severe for
922 human tolerance. *Science Advances* **6**, eaaw1838 (2020).

923 30.Yang, Y., Liu, G., Li, Y., Liao, X. & Li, Y. Misalignment between objective and perceived heat
924 risks. *Nat. Clim. Chang.* **15**, 1261–1263 (2025).

925 31.Berry, H. L., Waite, T. D., Dear, K. B. G., Capon, A. G. & Murray, V. The case for systems
926 thinking about climate change and mental health. *Nature Clim Change* **8**, 282–290 (2018).

927 32.Shannon, P. D. *et al.* Adaptation strategies and approaches for forested watersheds. *Climate*
928 *Services* **13**, 51–64 (2019).

929 33.Ji, H. *et al.* Research on adaption to air pollution in Chinese cities: Evidence from social media-
930 based health sensing. *Environmental Research* **210**, 112762 (2022).

931 34.Thompson, R., Hornigold, R., Page, L. & Waite, T. Associations between high ambient
932 temperatures and heat waves with mental health outcomes: a systematic review. *Public Health*
933 **161**, 171–191 (2018).

934 35.Waldock, K. A. M., Hayes, M., Watt, P. W. & Maxwell, N. S. Physiological and perceptual
935 responses in the elderly to simulated daily living activities in UK summer climatic conditions.
936 *Public Health* **161**, 163–170 (2018).

937 36.Adger, W. N. *et al.* Are there social limits to adaptation to climate change? *Climatic Change* **93**,

335–354 (2009).

37. Mora, C. *et al.* Global risk of deadly heat. *Nature Clim Change* **7**, 501–506 (2017).

38. Solecki, W. *et al.* City transformations in a 1.5 °C warmer world. *Nature Clim Change* **8**, 177–181 (2018).

39. Wolf, J., Adger, W. N., Lorenzoni, I., Abrahamson, V. & Raine, R. Social capital, individual responses to heat waves and climate change adaptation: An empirical study of two UK cities. *Global Environmental Change* **20**, 44–52 (2010).

40. Moser, S. C. Communicating climate change: history, challenges, process and future directions. *WIREs Climate Change* **1**, 31–53 (2010).

41. Hallegatte, S., Green, C., Nicholls, R. J. & Corfee-Morlot, J. Future flood losses in major coastal cities. *Nature Clim Change* **3**, 802–806 (2013).

42. Yin, J. *et al.* Future socio-ecosystem productivity threatened by compound drought–heatwave events. *Nat Sustain* **6**, 259–272 (2023).

43. Zhang, B., Wang, S. & Slater, L. Anthropogenic climate change doubled the frequency of compound drought and heatwaves in low-income regions. *Commun Earth Environ* **5**, 715 (2024).

44. Markolf, S. A. *et al.* Interdependent Infrastructure as Linked Social, Ecological, and Technological Systems (SETSs) to Address Lock-in and Enhance Resilience. *Earth's Future* **6**, 1638–1659 (2018).

45. Davis, L. W. & Gertler, P. J. Contribution of air conditioning adoption to future energy use under global warming. *Proceedings of the National Academy of Sciences* **112**, 5962–5967 (2015).

46. Linkov, I. *et al.* Changing the resilience paradigm. *Nature Clim Change* **4**, 407–409 (2014).

47. McPhearson, T. *et al.* Scientists must have a say in the future of cities. *Nature* **538**, 165–166

(2016).

48. Hass, A. L., Runkle, J. D. & Sugg, M. M. The driving influences of human perception to extreme heat: A scoping review. *Environmental Research* **197**, 111173 (2021).

49. Shih, H.-M. *et al.* Chinese Psychological Counseling Corpus Construction for Valence-Arousal Sentiment Intensity Prediction. in *2024 27th Conference of the Oriental COCOSDA International Committee for the Co-ordination and Standardisation of Speech Databases and Assessment Techniques (O-COCOSDA)* 1–5 (2024). doi:10.1109/O-COCOSDA64382.2024.10800036.

50. Scheffer, M. *et al.* Early-warning signals for critical transitions. *Nature* **461**, 53–59 (2009).

51. White, M. P. *et al.* Nature-based biopsychosocial resilience: An integrative theoretical framework for research on nature and health. *Environment International* **181**, 108234 (2023).

52. Hundessa, S. *et al.* Global excess deaths associated with heatwaves in 2023 and the contribution of human-induced climate change. *The Innovation* **6**, 101110 (2025).

53. Qiao, R. *et al.* Understanding the global subnational migration patterns driven by hydrological intrusion exposure. *Nat Commun* **15**, 6285 (2024).

Supplementary Files

This is a list of supplementary files associated with this preprint. Click to download.

- Supplementaryinformation.pdf